

Impacts of Hurricane Irma (2017) on ocean transport processes

Thomas Dobbelaere^{a,*}, Milan Curcic^b, Matthieu le Hénaff^{c,d}, Emmanuel Hanert^{a,e}

^a*Eath and Life Institute (ELI), UCLouvain, Louvain-la-Neuve, Belgium*

^b*Rosenstiel School of Marine and Atmospheric Sciences (RSMAS), University of Miami, Coral Gables, Florida, USA*

^c*Cooperative Institute for Marine and Atmospheric Studies (CIMAS), University of Miami, Miami, Florida, USA*

^d*Atlantic Oceanographic and Meteorological Laboratory (AOML), NOAA, Miami, Florida, USA*

^e*Institute of Mechanics, Materials and Civil Engineering (IMMC), UCLouvain, Louvain-la-Neuve, Belgium*

Abstract

In most hydrodynamic model studies, currents and waves are simulated in an uncoupled manner. These modelled currents can then be used to simulate the trajectories of passive drifters (pollutants, sediments, larvae, etc.) without taking wave or wave-current interactions into account. Although this simplification holds for most situations, as the force exerted by waves on currents can be neglected in fair weather conditions, it may lead to significant errors during storm conditions, when currents are strongly influenced by wind-generated waves. In this study, we investigate current-wave interactions in heavy-wind conditions and their impact on transport by coupling the unstructured-mesh hydrodynamic model SLIM with the spectral wave model SWAN. We apply the coupled model in the Florida Reef Tract during Hurricane Irma (Sep. 2017) and show that it successfully reproduces both the observed wave behavior and storm surge during the passage of the hurricane. The modeled currents are

*Corresponding author

Email address: thomas.dobbelaere@uclouvain.be (Thomas Dobbelaere)

then used to simulate the trajectories of passive drifters during the passage of the hurricane. Our results show that taking wave force into account induces variations of up 1 m/s in modelled currents on the continental shelf break as well as in the vicinity of reefs and islands. Wave-current interactions can therefore deflect the trajectories of drifting material by up to 10 km on the passage of the storm *Add something?*. These results strongly advocate for the inclusion of wave forces while studying transport processes (sediments, pollutants, larvae, etc.) in heavy-wind conditions.

Keywords:

1. Introduction

Wave-current interactions in coastal areas are of great importance for coastal engineering and management as they play a key role in sediment transport, morphological evolution and pollutant mixing (Bever and MacWilliams, 2013; Li and Johns, 1998). However, these interactions are highly nonlinear and can vary significantly in space and time (Wu et al., 2011). Wave-induced currents are generated by wave radiation stress gradients (Longuet-Higgins, 1970), affecting water levels near shorelines and wave breaking points (Longuet-Higgins and Stewart, 1964). Changes in water levels and currents, in turn, affect the motion and evolution of the waves (Sikirić et al., 2013). Coupled wave-current models are therefore required to correctly represent these complex interactions.

As coastal oceans are characterized by a complex topography with islands, inlets and estuaries, unstructured models are preferred as structured grid models show limitations in resolving topologically-controlled nearshore processes (Wu et al., 2011; Chen et al., 2007). Being able to capture the impact of topology on wave interactions becomes even more important in the case of hurricanes. The strong hurricane-induced winds generate large wind-waves and disturb ocean conditions (Liu et al., 2020) by causing coastal upwellings on continental shelves (Smith, 1982) and inducing strong currents, waves and

21 storm surges in nearshore and coastal regions (Dietrich et al., 2010; Weisberg
22 and Zheng, 2006).

23 South Florida and the Gulf of Mexico are particularly vulnerable to
24 hurricanes (Malmstadt et al., 2009) and modelling studies predict tropical
25 cyclones to increase both in frequency and intensity in this region (Marsooli
26 et al., 2019; Knutson et al., 2010). Accurately representing wave-current
27 interactions under strong winds becomes therefore critical in order to predict
28 hurricane impacts in events such as the Deepwater Horizon oil spill in
29 the Gulf of Mexico in 2010 (Le Hénaff et al., 2012). A better description of
30 the impacts of waves on currents could also improve the accuracy of search
31 and rescue efforts during storms (Breivik et al., 2013) or inform reef managers
32 by better understanding the impact of hurricane-induced currents on larval
33 dispersal (Lugo-Fernández et al., 2001).

34 Individual-based modelling of particulates has been extensively used to
35 study the transport of drifting materials such as pollutants, sediments or
36 larvae (Le Hénaff et al., 2012; Liubartseva et al., 2018; Figueiredo et al.,
37 2013; Frys et al., 2020). Although some of these studies take the impact of
38 waves into account by adding a Stokes drift velocity, *i.e.* the net drift of a
39 floating particle in the direction of the wave propagation (Van Den Bremer
40 and Breivik, 2018), to the Eulerian currents, they usually neglect the wave-
41 induced currents. Such practice is reasonable in the case of fair weather,
42 when wave-induced forces exerted on currents are relatively small, but might
43 lead to significant inaccuracies during storm conditions (Röhrs et al., 2012;
44 Curcic et al., 2016). To assess the importance of wave-current interactions
45 during a tropical cyclone, we investigated the transport of drifting particles
46 on the Florida shelf during Hurricane Irma, one of the strongest and costliest
47 tropical cyclones on record in the Atlantic Basin (Xian et al., 2018), which
48 made landfall in Florida in September 2017.

49 In this study, we developed an unstructured coupled wave-current model of
50 South Florida to simulate the ocean circulation during hurricane Irma. Both

51 modelled currents and waves were validated against field measurements and
52 were then used to simulate the transport of drifting material in the Florida
53 Keys and the Florida inner shelf during the passage of the hurricane. Model
54 outputs were then compared with uncoupled simulation results in order to
55 assess the impact of wave-induced forces and Stokes drift on the modelled
56 currents and transports.

57 **2. Methods**

58 *2.1. Study area and observational data*

59 The large-scale ocean circulation around South Florida is dominated by
60 the Florida Current (FC), which originates from the Loop Current (LC) where
61 it enters the Florida Straits from the Gulf of Mexico, and, downstream, forms
62 the Gulf Stream. The FC is a major western boundary current characterized
63 by spatial variability and meandering, associated with the presence of cyclonic
64 eddies between the core of the current and the complex reef topography of the
65 Florida Reef Tract (FRT) (Lee et al., 1995; Kourafalou and Kang, 2012). The
66 northern half of these reefs are made of early Holocene reef frameworks and
67 indurated sand ridges while the southern part (the Florida Keys) is composed
68 of a chain of limestone islands, fossilized remnants of ancient coral reefs and
69 sand bars (Hoffmeister and Multer, 1968; Shinn, 1988; Lidz and Shinn, 1991).
70 The variability of the FC extends over a large range of spatial and temporal
71 scales, with periods of 30-70 days in the Lower Keys (Lee et al., 1995) and
72 shorter periods of 2-21 days in the Upper Keys (Lee and Mayer, 1977), and
73 exhibits significant seasonal and interannual cycles (Johns and Schott, 1987;
74 Lee and Williams, 1988; Schott et al., 1988). Circulation on the West Florida
75 Shelf (WFS) on the other hand is forced by local winds and tidal fluctuations
76 (Lee and Smith, 2002; Liu and Weisberg, 2012).

77 The state of the ocean around Florida is monitored by an extensive
78 array of tide gauges, current meters and buoys. In this study, we used sea
79 surface elevation measurements from the National Oceanic and Atmospheric

80 Administrations (NOAA) Tides and Currents dataset. These measurements
81 were taken at four locations: two in the Florida Keys (Key West and Vaca Key);
82 one on the eastern coast of Florida (Virginia Key); and one on the western
83 coast (Naples). For the currents, we used ADCP measurements from the
84 University of South Florida's College of Marine Science's (USF/CMS) Coastal
85 Ocean Monitoring and Prediction System (COMPS) for the WFS (Weisberg
86 et al., 2009). More specifically, we used measurements from moorings C10,
87 C12 and C13, respectively located at the 25, 50, and 50 m isobaths of the
88 WFS (Liu et al., 2020). Finally, for the waves, we used measurements from
89 four buoys of the NOAA's National Data Buoy Center (NDBC); two on
90 Florida's eastern shelf and two on the WFS. The locations of all measurement
91 stations are shown in Fig. 1A,C.

92 *2.2. Wind and atmospheric pressure during Hurricane Irma*

93 Irma made landfall in Florida on 10 September 2017 as a category 3
94 hurricane, first at Cudjoe Key (Florida Keys) and later on Marco Island,
95 south to Naples (see hurricane track in Fig. 1). It then weakened to a
96 category 2 hurricane as it moved further inland (Pinelli et al., 2018). The
97 storm damaged up to 75% of the buildings at his landfall point in the Florida
98 Keys, making it one of the strongest and costliest hurricanes on record in the
99 Atlantic basin (Xian et al., 2018; Zhang et al., 2019). The strongest reported
100 wind speed was 50 m/s on Marco Island while the highest recorded storm
101 surge was 2.3 m, although larger wind speed likely occurred in the Florida
102 Keys (Pinelli et al., 2018). In order to reproduce the wind profile of Irma in
103 our model, we used high-resolution H*Wind wind fields (Powell et al., 1998).
104 As these data represent 1-min averaged wind speeds, we multiplied them by
105 a factor 0.93 to obtain 10-min averaged wind speeds (Harper et al., 2010),
106 which are more consistent with the time step of our model. Furthermore,
107 H*Wind wind profiles did not cover the whole model extent during the passage
108 of the hurricane and were thus blended within coarser wind field extracted
109 from ECMWF ERA-5 datasets (Fig. 2A). Pressure fields of Irma were also

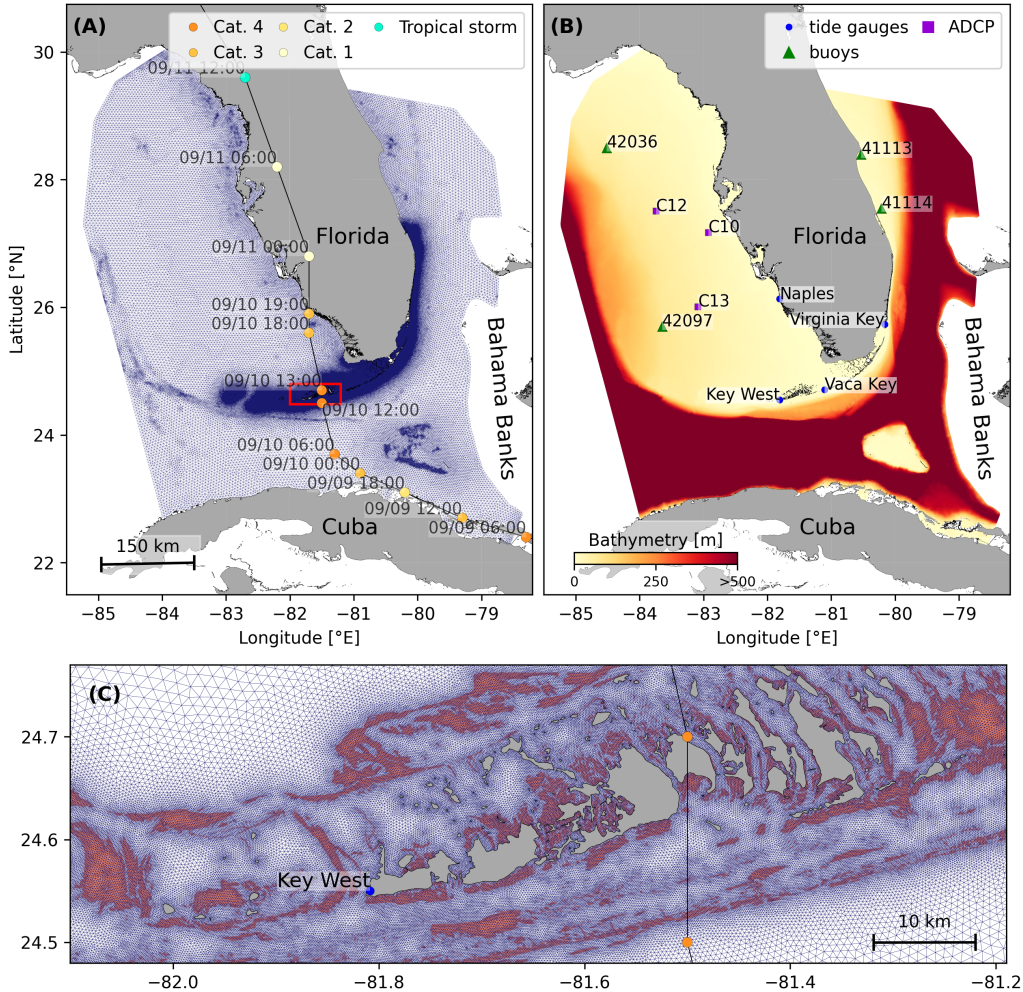


Fig. 1: **A:** Mesh of the computational domain with the trajectory of Irma, category of the hurricane is given by the Saffir-Simpson color scale. **B:** Bathymetry of the domain with the location of stations used for the validation of the model outputs. **C:** Close up view of the Lower Keys area, where the mesh resolution reaches 100m near reefs (shown in dark orange) and islands (highlighted in dark grey)

110 constructed using ERA-5 data. However, the coarse resolution of the dataset
 111 smoothes out the depression at the center of the hurricane, leading to an
 112 underestimation of the pressure gradient (Fig. 2B). To better capture the
 113 central depression of Irma, we built a hybrid pressure field using the position
 114 and the minimal pressure of the core of the hurricane based on its track as
 115 recorded in the HURDAT 2 database (Landsea and Franklin, 2013). Based on
 116 this information, the hybrid pressure field was constructed by combining an
 117 idealized Holland pressure profile (Lin and Chavas, 2012) within the radius of
 118 maximum wind speed of Irma (Knaff et al., 2018) with ERA-5 pressure field.
 119 The transition from the Holland profile to ERA-5 data outside the radius of
 120 maximum wind speed data was performed using a smooth step function (Fig.
 121 2).

122 *2.3. Hydrodynamic model*

123 Ocean currents generated during hurricane Irma around South Florida
 124 were modelled using the 2D barotropic version of the unstructured-mesh
 125 coastal ocean model SLIM¹. The model mesh covers an area similar to the
 126 model extent of Dobbelaere et al. (2020b), that includes the FRT but also the
 127 Florida Straits and part of the Gulf of Mexico (Figure 1). However, this area
 128 has been slightly extended northeastward and westward in order to include
 129 the NOAA-NDBC buoys. Furthermore, to withstand potential cell drying
 130 during the hurricane, we solved the conservative shallow water equations with
 131 wetting-drying:

$$\begin{aligned}
 \frac{\partial H}{\partial t} + \nabla \cdot (\mathbf{U}) &= 0 , \\
 \frac{\partial \mathbf{U}}{\partial t} + \nabla \cdot \left(\frac{\mathbf{U}\mathbf{U}}{H} \right) &= -f\mathbf{e}_z \times \mathbf{U} + \alpha g H \nabla(H - h) - \frac{1}{\rho} \nabla p_{\text{atm}} + \frac{1}{\rho} \boldsymbol{\tau}_s \quad (1) \\
 &\quad + \nabla \cdot (\nu \nabla \mathbf{U}) - \frac{C_b}{H^2} |\mathbf{U}| \mathbf{U} + \gamma (\mathbf{U}_{\text{ref}} - \mathbf{U}) ,
 \end{aligned}$$

¹<https://www.slim-ocean.be>

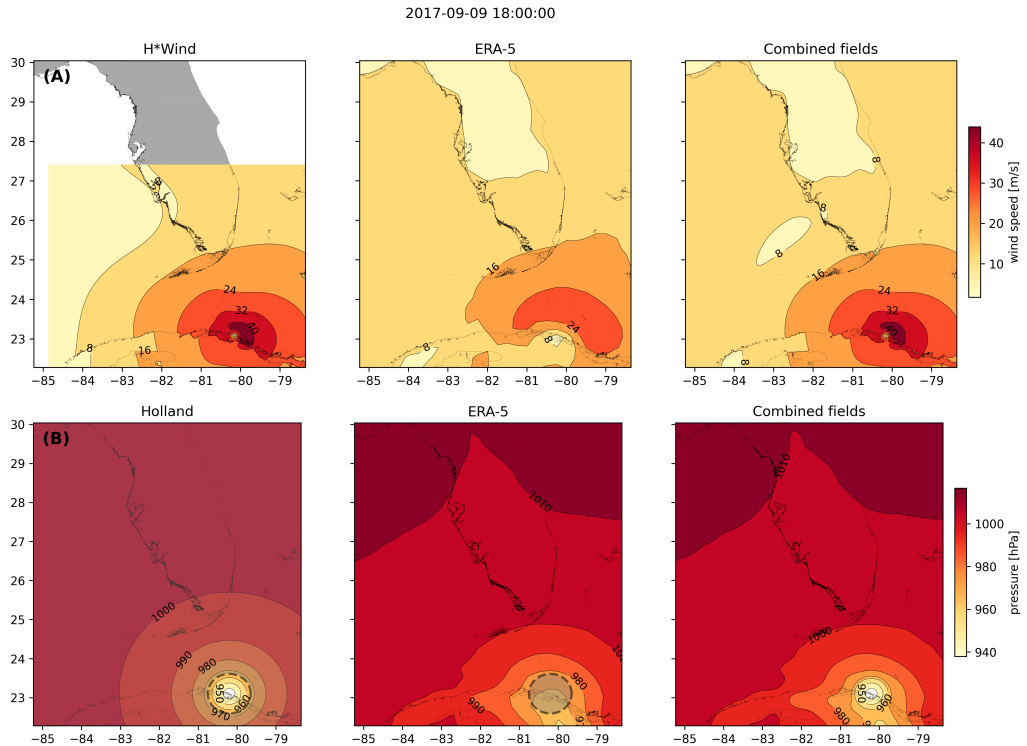


Fig. 2: Snapshot of the hybrid wind and pressure profiles constructed to capture the passage of Hurricane Irma at 1800 UTC 9 September 2017. Wind profiles are obtained by combining high resolution H*Wind with coarse ERA-5 wind fields. Pressure fields are built by combining RA-5 pressure field with an idealized Holland pressure profile based on the track of Irma in the HURDAT 2 database. Holland field was only used within the radius of maximum wind speed (discontinuous grey line) of the hurricane to capture its central depression.

132 where H is the water column height and \mathbf{U} is the depth-averaged transport;
 133 f is the Coriolis coefficient; g is the gravitational acceleration; h is the
 134 bathymetry; α is a coefficient stating whether the mesh element is wet ($\alpha = 1$)
 135 or dry ($\alpha = 0$) *[add more detail about impact of wetting-drying ?]*; ν is the
 136 viscosity; C_b is the bulk bottom drag coefficient; ∇p_{atm} is the atmospheric
 137 pressure gradient; τ_s is the surface stress, usually due to wind; and γ is a
 138 relaxation coefficient towards a reference transport \mathbf{U}_{ref} . As in Frys et al.
 139 (2020) and Dobbelaere et al. (2020b), SLIM currents were gradually relaxed
 140 towards the operational Navy HYCOM product (GOMl0.04², Chassignet et al.
 141 (2007)) in regions where the water depth exceeds 50m.

142 At very high wind speeds, the white cap is blown off the crest of the waves
 143 (also known as spumes), which has been hypothesized to generate a layer
 144 of droplets that acts as a slip layer for the winds at the ocean-atmosphere
 145 interface (Holthuijsen et al., 2012). This causes a saturation of the wind drag
 146 coefficient for strong winds (Powell et al., 2003; Donelan et al., 2004; Curcic
 147 and Haus, 2020). We take this saturation effect into account by using the wind
 148 drag parameterization of Moon et al. (2007). In this parameterization, the
 149 drag coefficient C_d depends on the wind speed at 10-m height U_{10} according
 150 to:

$$C_d = \kappa^2 \log \left(\frac{10}{z_0} \right)^{-2} \quad (2)$$

151 where κ is the von Karman constant and z_0 is the roughness length expressed
 152 as:

$$z_0 = \begin{cases} \frac{0.0185}{g} U_*^2 & \text{if } U_{10} \leq 12.5 \text{ m/s ,} \\ [0.085(-0.56U_*^2 + 20.255U_* + 2.458) - 0.58] \times 10^{-3} & \text{if } U_{10} > 12.5 \text{ m/s ,} \end{cases} \quad (3)$$

²<https://www.hycom.org/data/goml0pt04>

153 with U_* the friction velocity. The relation between U_{10} and U_* is given by:

$$U_{10} = -0.56U_*^2 + 20.255U_* + 2.458 . \quad (4)$$

154 The mesh resolution depends on the distance to coastlines and reefs
155 following the approach of Dobbelaere et al. (2020b). The mesh is then further
156 refined according to bathymetry value and gradient, as suggested in the
157 SWAN user-guide³. Such an approach improves the model efficiency as the
158 mesh resolution is only increased where required by the currents and waves
159 dynamics. The mesh was generated with the seamsh⁴ Python library, which is
160 based on the open-source mesh generator GMSH (Geuzaine and Remacle,
161 2009). It is composed of approximately 7.7×10^5 elements. The coarsest
162 elements, far away from the FRT, has a characteristic length of about 5 km
163 whereas the finest elements have a characteristic length of about 100 m along
164 the coastlines and over the reefs (Fig 1).

165 *2.4. Wave model*

166 Waves were modelled using the parallel unstructured-mesh version of the
167 Simulating WAves Nearshore (SWAN) model (Booij et al., 1999), one of the
168 most commonly used wave models in coastal areas and inland waters. This
169 model solves the action balance equation (Mei, 1989):

$$\frac{\partial N}{\partial t} + \nabla_{\mathbf{x}} \cdot [(\mathbf{c}_g + \mathbf{u})N] + \frac{\partial}{\partial \theta}[c_\theta N] + \frac{\partial}{\partial \sigma}[c_\sigma N] = \frac{S_{in} + S_{ds} + S_{nl}}{\sigma} , \quad (5)$$

170 where $N = E/\sigma$ is the wave action density and E is the wave energy spectrum;
171 θ is the wave propagation direction; σ is the intrinsic wave frequency; \mathbf{c}_g is
172 the wave group velocity, $\mathbf{u} = \mathbf{U}/H$ is SLIM depth-averaged current velocity;
173 c_θ and c_σ are the propagation velocities in spectral space due to refraction
174 and shifting in frequency due to variations in depth and currents; and S_{in} ,

³<http://swanmodel.sourceforge.net/unswan/unswan.htm>

⁴<https://pypi.org/project/seamsh/>

S_{ds}, and *S_{nl}* respectively represent wave growth by wind, wave decay and nonlinear transfers of wave energy through interactions between triplets and quadruplets. The wave spectra were discretized with 48 direction bins and 50 frequency bins logarithmically distributed from 0.03 to 2 Hz. Exponential wind growth was parameterized using the formulation of Janssen (1991), while dissipations by whitecapping and bottom dissipations followed the formulations of Komen et al. (1984) and Madsen et al. (1989), respectively. Coefficients for exponential wind growth and whitecapping parameterizations were based on the results of Siadatmousavi et al. (2011), and significantly differ from SWAN's default settings. By default, SWAN implements the wind input formulation of Komen et al. (1984) and the steepness-dependent coefficient governing dissipation by whitecapping is a linear function of the wave number. In this study, this steepness-dependent coefficient is a quadratic function of the wave number, as it showed better predictions of the significant wave height in the study of Siadatmousavi et al. (2011). The choice of these formulations was motivated by the appearance of numerical instabilities in the region of the Gulf Stream when using SWAN's default parameter values. Finally, wave boundary conditions were derived from WAVEWATCH III (Tolman et al., 2009) spectral outputs at NDBC buoy locations. We selected these datasets as the large number of NDBC buoys around our region of interest allowed for a fine representation of the wave spectra on the boundary of the domain.

Surface waves induce a net drift in the direction of the wave propagation, known as the Stokes drift (Van Den Bremer and Breivik, 2018; Stokes, 1880). This net drift has a significant impact on sediment transport in nearshore regions (Hoefel and Elgar, 2003), on the formation of Langmuir cells (Langmuir, 1938; Craik and Leibovich, 1976) as well as on the transport of heat, salt or pollutants such as oil or micro-plastic in the upper ocean layer (McWilliams and Sullivan, 2000; Röhrs et al., 2012; Drivdal et al., 2014). To correctly model the Stokes drift profile in mixed wind-driven sea and swell

205 conditions, the full two-dimensional wave spectrum must be represented by a
 206 spectral wave model within a wave-current coupling (Van Den Bremer and
 207 Breivik, 2018). We therefore used SWAN modelled spectra to compute the
 208 Stokes drift as follows:

$$\mathbf{u}_s = \int_0^{2\pi} \int_0^{+\infty} \frac{\sigma^3}{h \tanh(2kh)} E(\sigma, \theta) (\cos \theta, \sin \theta) d\sigma d\theta , \quad (6)$$

209 where k is the norm of the wave vector; h is the water depth; and $E(\sigma, \theta)$ is
 210 the wave energy density.

211 *2.5. Coupled model*

212 SLIM and SWAN are coupled so that they run on the same computational
 213 core and the same unstructured mesh. SLIM is run first and passes the
 214 wind velocity (\mathbf{U}_{10}), water level ($\eta = H - h$) and depth-averaged current
 215 ($\mathbf{u} = \mathbf{U}/H$) fields to SWAN, as well as a roughness length (z_0) for the bottom
 216 dissipation formulation of Madsen et al. (1989). This roughness length is
 217 computed from SLIM's bulk drag coefficient C_b following the approach of
 218 Dietrich et al. (2011) so that both models have consistent bottom dissipation
 219 parameterizations. SWAN then uses these quantities to compute the wave
 220 radiation stress gradient, that is then passed to SLIM as the force exerted
 221 by waves on currents $\boldsymbol{\tau}_{\text{wave}}$ (Fig. 3). SLIM then uses this quantity to
 222 update the value of the surface stress $\boldsymbol{\tau}_s$ in Eq. (1), that now becomes
 223 the sum of wind and wave-induced stresses $\boldsymbol{\tau}_s = \boldsymbol{\tau}_{\text{wind}} + \boldsymbol{\tau}_{\text{wave}}$. Here, the
 224 momentum flux from the atmosphere to the ocean is taken as the commonly-
 225 used full wind stress $\boldsymbol{\tau}_{\text{wind}}$. Doing so, we neglect the momentum advected
 226 away from the storm by the waves, leading to a 10-15% overestimation of
 227 the momentum flux in hurricane winds Curcic (2015). Moreover, we followed
 228 the approach of Dietrich et al. (2012) by characterizing the wave-induced
 229 stresses using the radiation-stress representation instead of the vortex-force
 230 representation (McWILLIAMS et al., 2004). Although the later provides a
 231 clearer and meaningful decomposition of the wave-effect, we implemented the

232 first representation for the sake of simplicity as it allows us to provide the
233 whole wave contribution as an additional surface stress to SLIM (Lane et al.,
234 2007).

235 SLIM's governing equations are integrated using an implicit time integra-
236 tion scheme while SWAN is unconditionally stable (Dietrich et al., 2012),
237 allowing both models to be run with relatively large time steps. In this study,
238 the stationary version of SWAN was used, *i.e.* the time derivative of Eq. 5
239 was set to zero. This resulted in reduced scaling and convergence rates than
240 with the nonstationary version of SWAN but increased the stability of the
241 model. The wave spectra at each node of the mesh was saved at the end of
242 each iteration to serve as initial conditions for the next one. Both models
243 were run sequentially using a time step of 600s, so that each computational
244 core was alternatively running either SLIM or SWAN. As in the coupling
245 between SWAN and ADCIRC (Dietrich et al., 2012), both models use the
246 same local sub-mesh, allowing for a one-to-one correspondence between the
247 geographic locations of the mesh vertices. No interpolation is therefore needed
248 when passing the discretised variables from one model to the other, which
249 allows an efficient inter-model communication. However, as SLIM applies
250 discontinuous Galerkin finite element methods, an additional conversion step
251 to a continuous framework was required to transfer SLIM nodal quantities to
252 SWAN.

253 3. Results

254 We first validated the reconstructed atmospheric fields of hurricane Irma
255 as well as the outputs of our coupled jave-current model against field mea-
256 surements. A summary of the error statistics is given in Table 1. We then use
257 the validated model to simulate the transport of passive drifters in the Lower
258 Keys during the passage of Hurricane Irma. These drifters were advected by
259 two sets of currents: (i) the currents from an uncoupled SLIM model run
260 during Irma (SLIM) and (ii) the currents from the coupled SLIM+SWAN

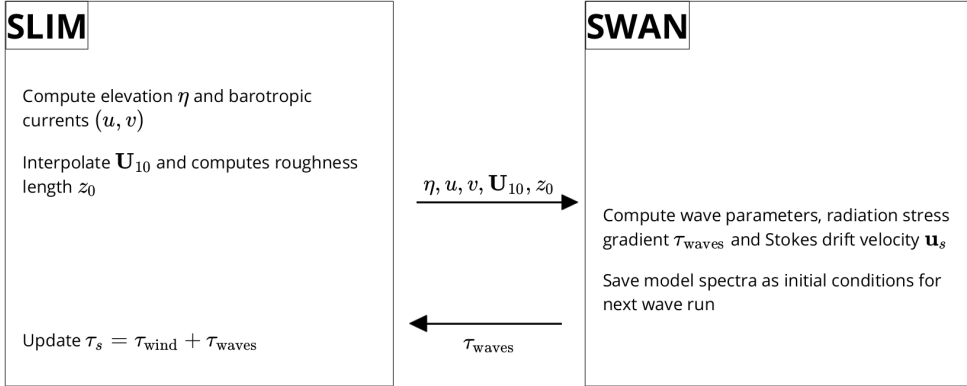


Fig. 3: Schematic illustration of the coupled SLIM+SWAN model.

model (SLIM+SWAN). Furthermore, the depth-averaged Stokes drift was computed using the wave spectra of our coupled model run (Stokes-C) as well as those of an uncoupled SWAN run during the passage of the hurricane (Stokes-U). We then simulated the trajectories of passive tracers during the passage of the Irma in the Lower Keys using different combinations of these fields. These trajectories were finally compared to evaluate the impact of the wave-current interactions and the Stokes drift on the transport processes during a major hurricane.

3.1. Model validation

H*Wind winds and hybrid pressure field agree well with station measurements at Vaca Key station (Fig. 4). The hybrid pressure field shows better agreement with observations than ERA-5 pressure as it successfully reproduces the storm depression. ERA-5 fields, on the other hand, fail to resolve the low pressure at the core of the hurricane due to their coarser grid, leading to an overestimation of 8 mbar of the storm depression. Both H*Wind and ERA-5 agree well with observed wind speeds although both data sets tend to slightly overestimate the width and intensity of the wind peak. However, H*wind profiles show a better match with the timing of the observed peak, as ERA-5 winds tend to anticipate it. H*wind also exhibits a

Validation of atmospheric forcings at Vaca Key station

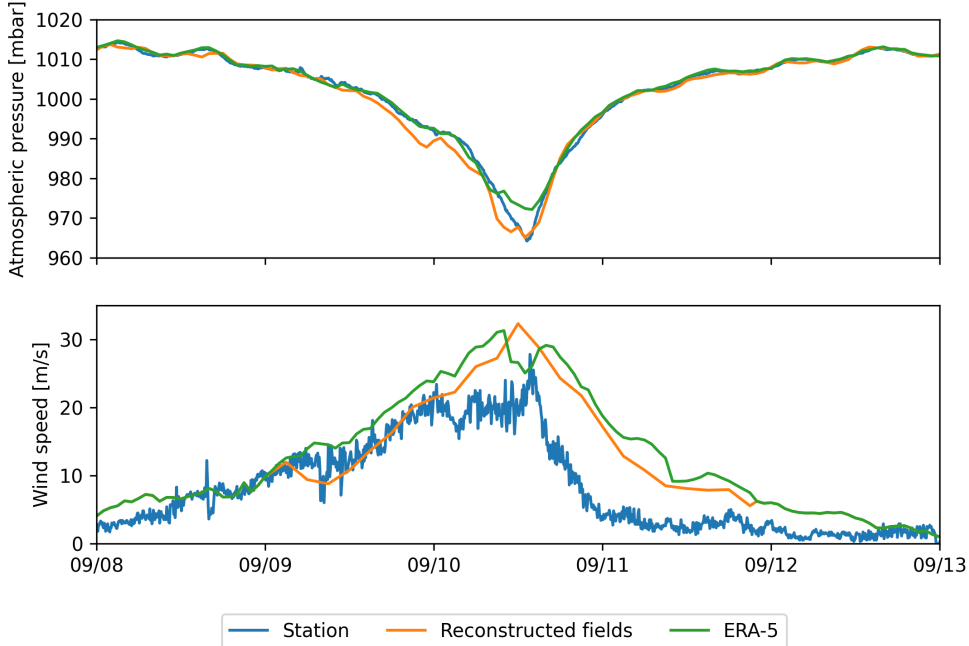


Fig. 4: Comparison of reconstructed wind atmospheric pressure with field measurements and coarser ECMWF ERA-5 profiles at Vaca Key station. The generated hybrid atmospheric forcings better capture the observed storm depression while H*wind winds better match the measured peak in wind speed.

slightly narrower peak in wind speed, which better agrees with observations.
 Hydrodynamic outputs of the coupled wave-current model agree well with tide gauge (Fig. 5) and ADCP measurements (Fig. 6). Despite a slight overestimation of the amplitude of sea surface elevation (1) in fair weather conditions, the timing and amplitude of the storm surges are well reproduced by the coupled model. The largest model error during the surge is an overestimation of 18 cm of the elevation peak at Virginia Key. The fit is especially good at Naples, where both the large positive and negative surges are captured by the coupled model with an error of less than 5 cm. Modelled 2D currents were validated against depth-averaged ADCP measurements at mooring station C10, C12 and C13 (Fig. 6). As in Liu

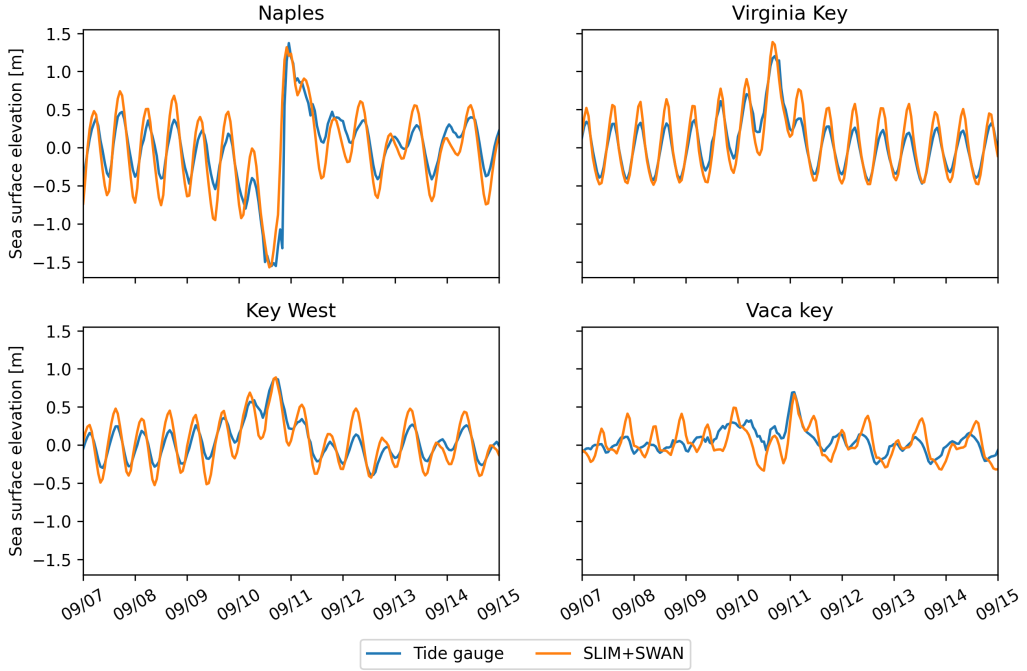


Fig. 5: Comparison of modelled sea surface elevation with all 4 tide gauge measurements (see Fig. 1B for their location). Timing and amplitudes of the storm surges are well reproduced by the model

et al. (2020), we performed the vector correlation analysis of Kundu (1976) to compare modelled and observed current velocity vectors. Correlation coefficients (ρ) between simulated and observed depth-averaged currents were 0.84, 0.74 and 0.73 at the C10, C12 and C13 locations, respectively. Average veering angles were computed as well and were below 12° , as in (Liu et al., 2020). Furthermore, Table 1 indicates that our model tends to produce larger prediction errors on the northward component of the depth-averaged currents than the eastward one. As expected from a depth-averaged model, the best fit with observations is obtained at the shallowest mooring C10, located on the 25 m isobath, with an average veering angle of 6° and smaller error statistics (Table 1).

The simulated significant wave height agrees well with observations on

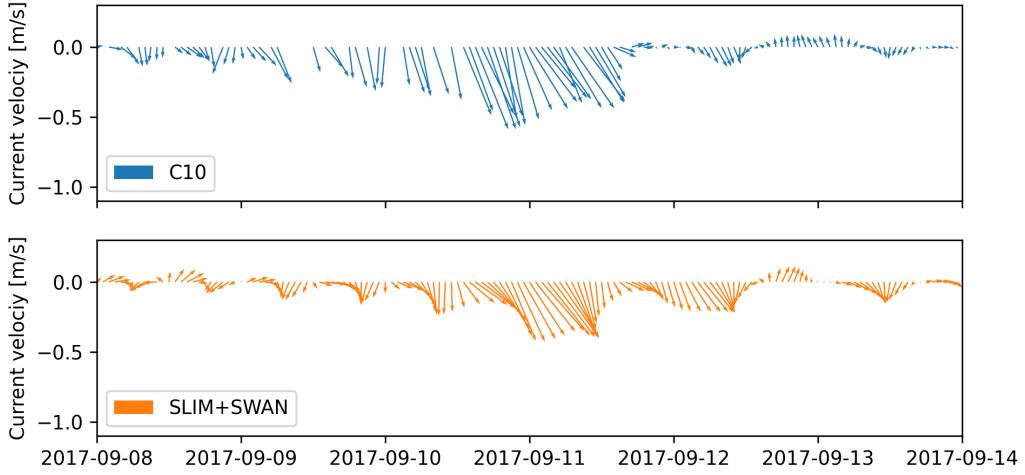


Fig. 6: Comparison of modelled current velocity with observed velocity at mooring C10 (see Fig. 1B for its location). Modelled current velocities agree well with observations, with a correlation coefficient of 0.83 and an average veering angle of 6° .

the WFS, where errors on the peak value do not exceed 5% (Fig. 7). On Florida's eastern shelf, errors are slightly larger and reach 20%. Although the model outputs agree well with observations, a lag in significant wave height is observed for all 4 buoys. Moreover, the peak in significant wave height tends to be underestimated at buoys 41113 and 41114, located on the East Florida Shelf. Other wave parameters were better reproduced by the model on the WFS as well (see buoy 42036 in Fig. 7 and Table 1).

3.2. Impact of waves on currents and transport

We evaluated the impact of wave-current interactions on modelled currents during the passage of Irma in the Lower Keys, between Sept. 7 and 13, 2017. First, we computed the maximum difference between currents modelled by SLIM and SLIM+SWAN during this period (Fig. 8A). The largest differences in current speed were observed over the reefs, on the shelf break and around islands. They can locally reach 1 m/s, with the coupled model SLIM+SWAN yielding the largest amplitudes. The regions where the differences are the largest experience the largest wave-induced stress τ_{wave} (Fig. 8B), as wave

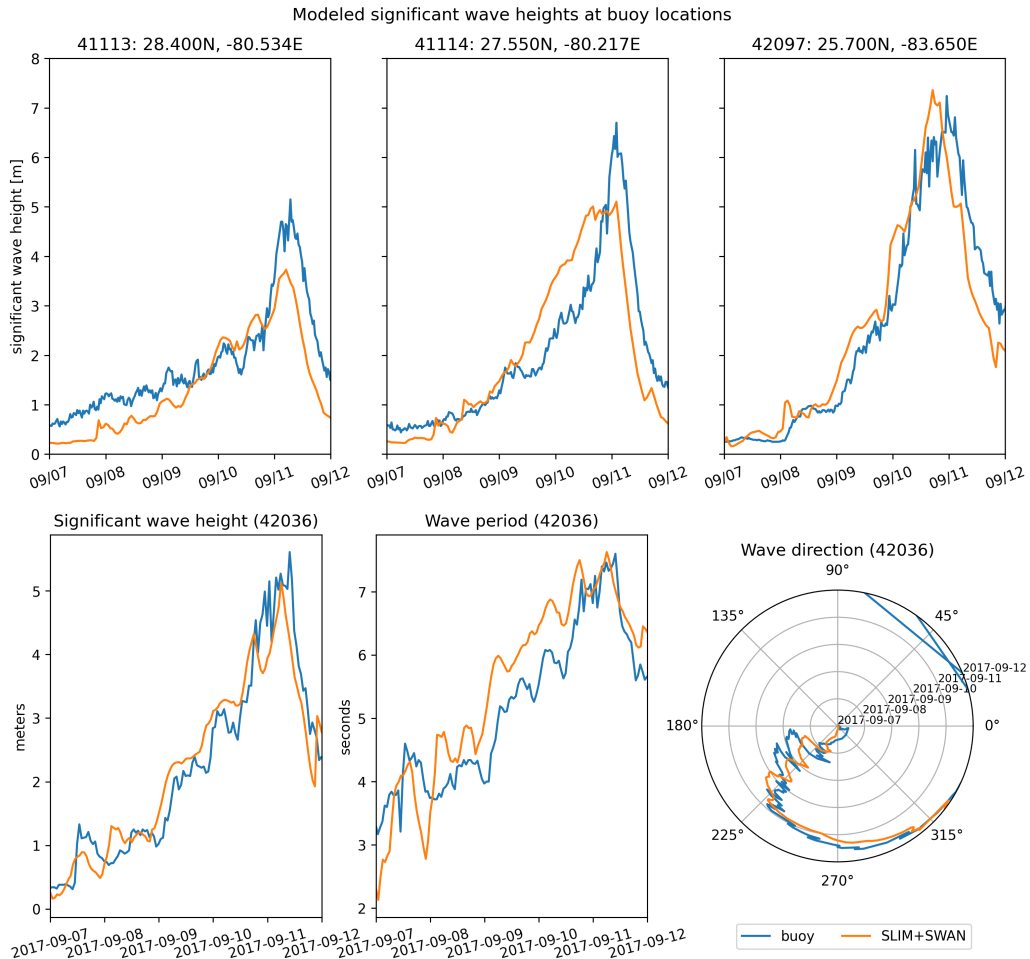


Fig. 7: Comparison of modelled wave parameters with observation at the 4 buoys location (locations shown in Fig. 1B). Modelled significant wave height agrees well with field measurement.

Station	Variable	Bias	MAE	RMSE
Vaca Key	sse (m)	n/a	0.12	0.16
	U_{10} (m/s)	1.51	1.85	2.61
	p_{atm} (hPa)	-0.21	0.59	1.03
Key West	sse (m)	n/a	0.11	0.13
Virginia Key	sse (m)	n/a	0.10	0.13
Naples	sse (m)	n/a	0.18	0.23
C10	u (m/s)	-0.006	0.04	0.05
	v (m/s)	0.02	0.06	0.08
C12	u (m/s)	-0.01	0.06	0.07
	v (m/s)	0.06	0.09	0.11
C13	u (m/s)	0.004	0.06	0.08
	v (m/s)	0.04	0.06	0.08
41113	H_s (m)	-0.35	0.40	0.51
	T_m (s)	-2.18	2.47	3.13
41114	H_s (m)	-0.21	0.53	0.68
	T_m (s)	-1.69	2.53	3.15
42036	H_s (m)	-0.03	0.26	0.36
	T_m (s)	0.04	0.65	0.77
42097	H_s (m)	-0.15	0.40	0.57
	T_m (s)	0.02	0.62	0.74

Table 1: Error statistics comparing SLIM+SWAN simulated quantities with the measured sea surface elevation (sse), eastward and northward depth-average current velocities (u,v), significant wave height (H_s), and zero-crossing mean wave period (T_m). Model bias, mean absolute error (MAE), and root mean squared error (RMSE) are listed by variable (unit) and value.

319 breaking and wave slowing down over rough seabed induce variations of the
320 wave radiation stress (Longuet-Higgins and Stewart, 1964). Wave-induced
321 differences in current speed were amplified by the action of the wind stress
322 τ_{wind} (Fig. 8C). Wind speeds were larger in the front right quadrant of the
323 hurricane (Zedler et al., 2009), yielding larger differences on the right-hand
324 side of the storm trajectory. This is especially clear in the area between
325 the Florida Keys and the Everglades, where relatively small values of τ_{wave}
326 nonetheless produce current speed differences of up to 0.5 m/s because of the
327 wind stress.

328 To quantify the impact of these differences in the velocity fields, we
329 compared the trajectories of passive particles advected by the uncoupled
330 SLIM and coupled SLIM+SWAN currents during the passage of Irma in the
331 Lower Keys (Fig. 9). Particles were released on the inner and outer shelves
332 at the points highlighted in red and blue dots in Fig. 9A on Sept. 7 at 0000
333 UTC and then tracked until Sept. 15. These areas were constructed using
334 backtracking methods (Dobbelaeere et al., 2020a) to ensure that the release
335 particles would intersect the path of Irma during its passage through the
336 Florida Keys. We first defined two 25km^2 circular regions on the trajectory of
337 the hurricane (see red and blue circles in Fig. 9A). Particles within these two
338 regions were then tracked backward in time using uncoupled SLIM currents
339 from the exact time of the passage of the hurricane until Sept. 7 at 0000
340 UTC. Their positions at the end of the backward simulation (see red and blue
341 particle clouds in Fig. 9) corresponds to the initial condition of the forward
342 transport simulations described below.

343 We compared the trajectories of particles originating from these regions
344 and advected forward in time by different sets of currents: (i) uncoupled SLIM
345 currents alone; (ii) coupled SLIM+SWAN currents; (iii) SLIM currents with
346 the addition of the depth-averaged Stokes drift computed with the coupled
347 wave-current model (Stokes-C); (iv) SLIM+SWAN currents with StokesC;
348 and (v) SLIM currents with the depth-averaged Stokes drift computed with

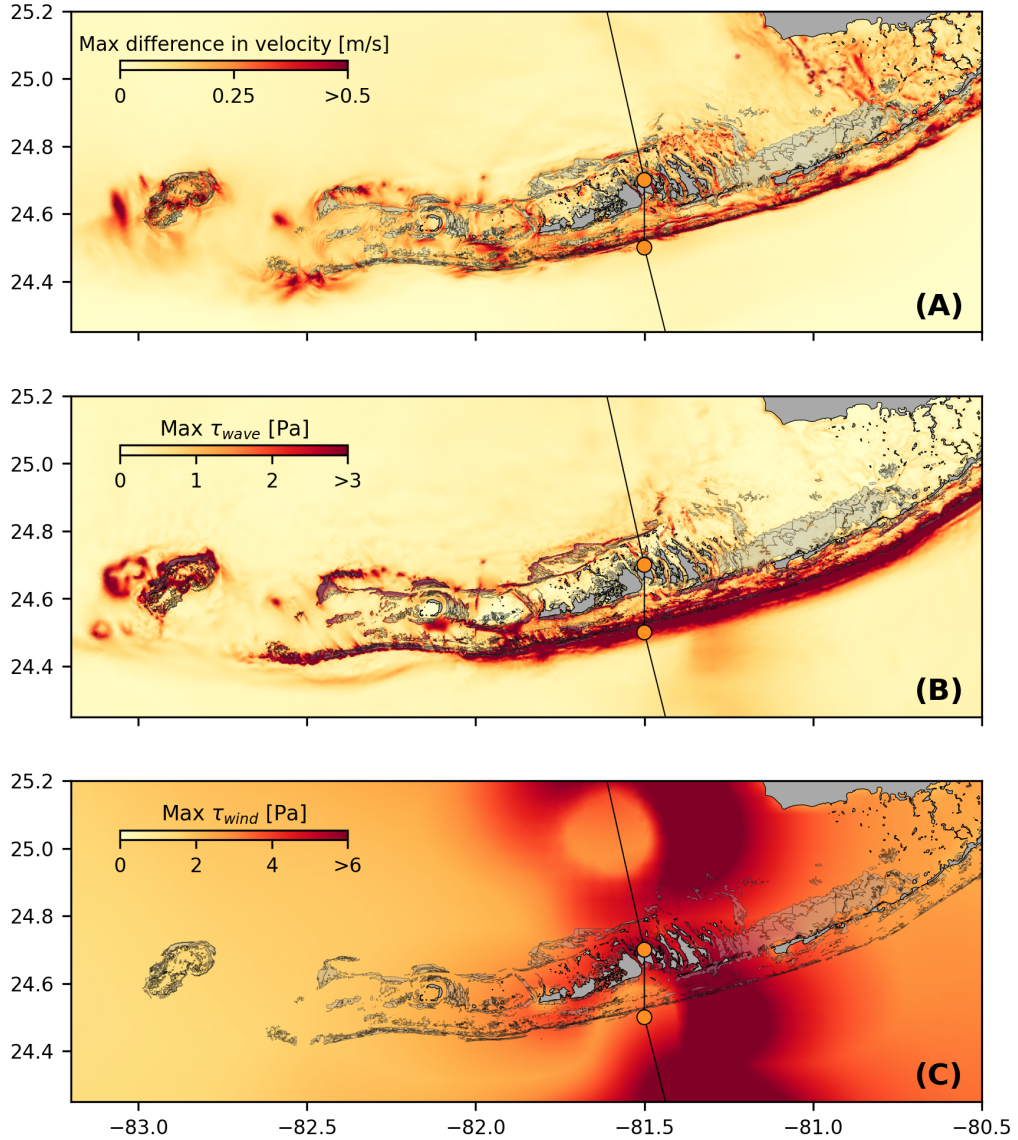


Fig. 8: Maximum difference between SLIM and SLIM+SWAN currents (A) during the passage of Irma in the Lower Florida Keys, along with the maximum wave radiation stress gradient τ_{wave} (B) and wind stress τ_{wind} (C) generated by the hurricane. Wave-induced stress yields difference larger than 0.5 m/s in current velocities.

349 the uncoupled wave model (Stokes-U). Particles trajectories are compared by
350 computing the distances between the centers of mass of the particle clouds
351 through time. The main result coming out of this analysis is that the waves
352 play a significant role on the transport processes during and after the passage
353 of hurricane Irma. Comparison of SLIM and SLIM+SWAN highlights that
354 wave-current interactions alone yield differences of up to 5 km between the
355 modelled trajectories on the passage of the hurricane. These differences exceed
356 10 km on the outer shelf when Stokes drift is taken into account (see 'SLIM
357 vs SLIM+SWAN+Stokes-C' and 'SLIM vs. SLIM+Stokes-C' in Fig. 9B).

358 The impact of the waves on the transport processes differs significantly
359 between the inner and outer shelves, with wave-induced differences in tra-
360 jectories 4 to 5 times larger on the outer shelf. Furthermore, the distances
361 between the centers of mass of the clouds of particles tend to stabilize after
362 the passage of Irma on the inner shelf, while they keep increasing up to
363 two days after the passage of the hurricane on the other shelf when taking
364 Stokes drift into account. These distances then stabilize for about a day
365 before they start decreasing (see top right panel of Fig. 9B). However, when
366 considering wave-current interactions alone (SLIM vs. SLIM+SWAN), this
367 decrease in distances occurs just after the passage of Hurricane Irma. These
368 larger distances between the modeled trajectories on the outer shelf can be
369 explained by the larger waves, current velocities and spatial variability in this
370 region. Furthermore, the fact that the differences between SLIM alone and
371 model runs including Stokes drift keep increasing after the passage of Irma
372 indicates that the impact of the hurricane on the wave field was still significant
373 on the outer shelf up to 2 days after it crossed the Florida Keys.

374 Comparison of 'SLIM vs. SLIM+SWAN' with the other curves in Fig
375 9B indicates that the effect of the Stokes drift dominates the impact of the
376 radiation stress gradient and the wave-current interactions. Nonetheless,
377 'SLIM vs. SLIM+SWAN' yields values similar to the other two curves on
378 the outer shelf on the passage of Hurricane Irma. This suggest that the

379 impact of waves on currents induce effects similar to the impact of the Stokes
380 drift during the passage of hurricane Irma on the outer shelf. However,
381 comparing SLIM and SLIM+SWAN both on the inner and other shelf, we
382 see that this impact is negligible during the rest of the simulation. Moreover,
383 comparison of Stokes-U and Stokes-C (bottom panels of Fig. 9B) indicates
384 that the difference between the trajectories of particles advected by the two
385 Stokes drift do not exceed 2 km, with larger discrepancies on the outer shelf.
386 The sudden increase of 'SLIM+Stokes-C vs SLIM+Stokes-U' curves on the
387 passage of Irma (and two days after on the outer shelf) and their stabilization
388 afterwards suggest that taking wave-currents interactions into account when
389 modeling waves mostly has an impact during (and directly after) the passage
390 of the hurricane.

391 4. Discussion

392 Ability of wave model to correctly capture gradient in significant wave
393 height due to current-waves interactions under tropical cyclones depends on:

- 394 • Broad perspective \Rightarrow not limited to FL
- 395 • Mention search and rescue
- 396 • However, ignoring waves in storm conditions could result in significant
397 inaccuracies in modelled trajectories, as illustrated in the case of release
398 region 2 in Fig. 9
- 399 • Spatial (10km \rightarrow 5km) and spectral (36 dir. \rightarrow 48 dir.) resolution
400 (Hegermiller et al., 2019)
- 401 • Directional spreading of incident waves (Villas Bôas et al., 2020)
- 402 • This result is of interest as negative surges, although less studied, affect
403 water exchanges between the estuaries and the coastal ocean and disturb
404 the benthic ecosystems (Liu et al., 2020)

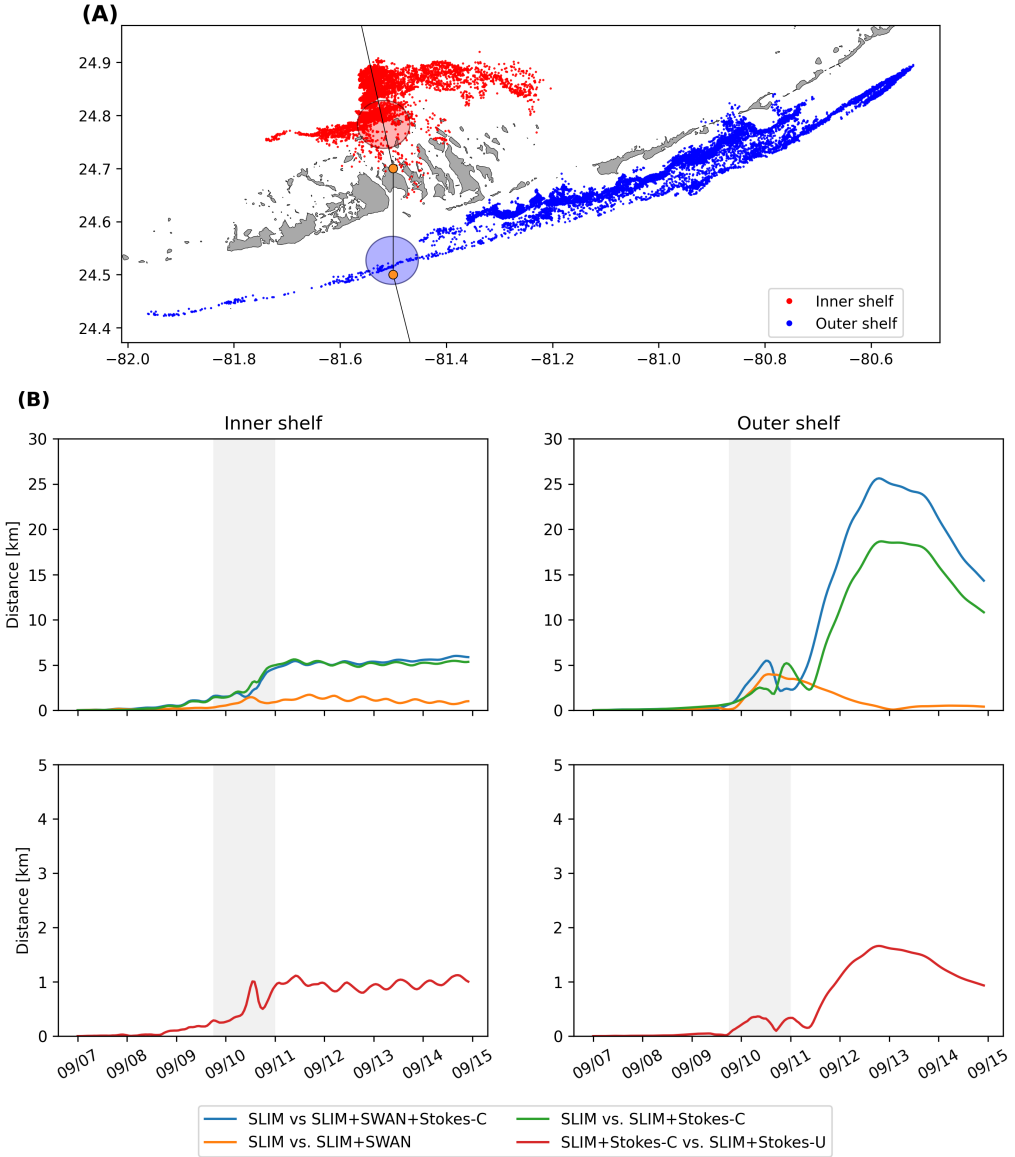


Fig. 9: **A:** Release regions of the passive particles on the inner and outer shelves (red and blue clouds) obtained by backtracking particles released in the red and blue circular areas during the passage of Irma. **B:** Difference between the centers of mass of the particle clouds released from the regions highlighted in **A** and advected by different combinations of coupled and uncoupled velocity fields. **Matthieu:** prsenter plus d'informations sur la Figure 8, notamment les nuages de points issus des deux simulations (SLIM et SLIM+SWAN+Stokes-C), ainsi que les centres de masses correspondants. Ca devrait permettre de soutenir la partie rsultats.

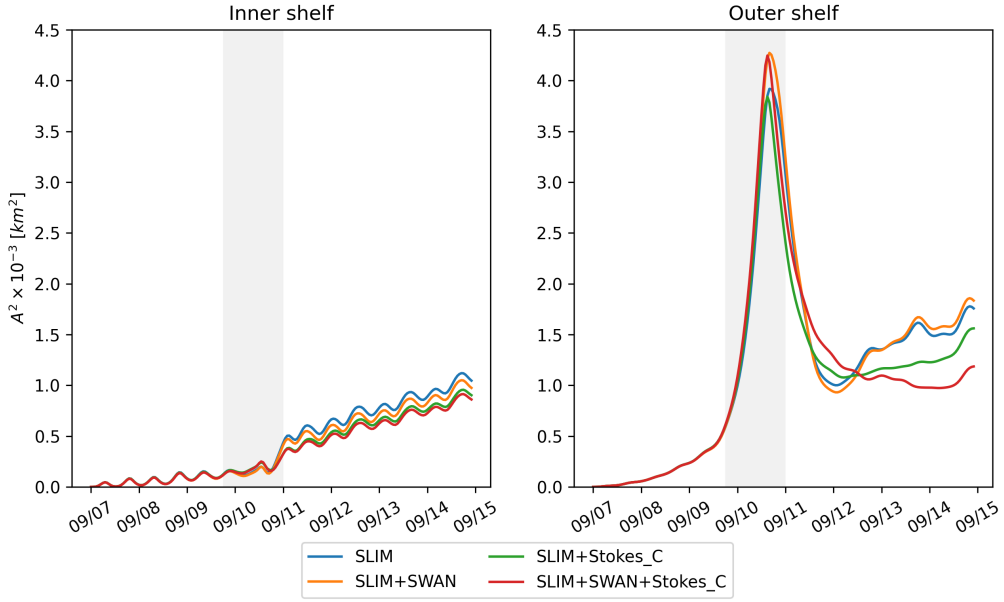


Fig. 10: Dispersion of particles with different velocity fields → not sure to know what to say about that...

- 405 • As model parameters were calibrated for the Northern Gulf of Mexico,
 406 observations are better reproduced at buoys located on the WFS, as
 407 illustrated for buoy 42036 + This good fit on the WFS is not surprising as
 408 the parameters used for wind energy input and whitecapping dissipation
 409 were based on the calibration performed by Siadatmousavi et al. (2011)
 410 on the Northern Gulf of Mexico. Wind-induced wave growth might
 411 therefore be underestimated on the eastern shelf. Consequently, incident
 412 wave do not receive enough energy to grow after breaking on the bank
 413 boundary, leading to an underestimation of the significant wave height
 414 at the location of the buoys. Nonetheless, as this study focused on the
 415 wave produced by Irma, which made landfall on the western coasts of
 416 Florida, the use of parameterizations calibrated for the Gulf of Mexico
 417 seems reasonable.
- 418 • This difference between the inner and outer shelf can be explained by

419 the sheltering of the inner shelf due to reefs and islands as well as wave
420 breaking on the shelf break. The inner shelf hence experiences weaker
421 waves and weaker currents, and hence also weaker and more localised
422 transport.

- 423
- 424 • Furthermore, as SLIM vs SLIM+SWAN+Stokes and SLIM vs. SLIM+Stokes-
425 C show similar values on the inner shelf, this suggests that the combina-
426 tion of currents and Stokes drifts produces sufficiently accurate results
on sheltered shallow areas such as the WFS

427 **5. Conclusion**

428 **Acknowledgments**

429 Computational resources were provided by the Consortium des Équipements
430 de Calcul Intensif (CÉCI), funded by the F.R.S.-FNRS under Grant No.
431 2.5020.11. Thomas Dobbelaere is a PhD student supported by the Fund for
432 Research training in Industry and Agriculture (FRIA/FNRS).

433 **References**

- 434 Bever, A.J., MacWilliams, M.L., 2013. Simulating sediment transport pro-
435 cesses in San Pablo Bay using coupled hydrodynamic, wave, and sediment
436 transport models. *Marine Geology* 345, 235–253.
- 437 Booij, N., Ris, R.C., Holthuijsen, L.H., 1999. A third-generation wave
438 model for coastal regions: 1. Model description and validation. *Journal of*
439 *geophysical research: Oceans* 104, 7649–7666.
- 440 Breivik, Ø., Allen, A.A., Maisondieu, C., Olagnon, M., 2013. Advances in
441 search and rescue at sea.
- 442 Chassignet, E.P., Hurlburt, H.E., Smedstad, O.M., Halliwell, G.R., Hogan,
443 P.J., Wallcraft, A.J., Baraille, R., Bleck, R., 2007. The HYCOM (hybrid

- 444 coordinate ocean model) data assimilative system. Journal of Marine
445 Systems 65, 60–83.
- 446 Chen, C., Huang, H., Beardsley, R.C., Liu, H., Xu, Q., Cowles, G., 2007.
447 A finite volume numerical approach for coastal ocean circulation studies:
448 Comparisons with finite difference models. Journal of Geophysical Research:
449 Oceans 112.
- 450 Craik, A.D., Leibovich, S., 1976. A rational model for Langmuir circulations.
451 Journal of Fluid Mechanics 73, 401–426.
- 452 Curcic, M., 2015. Explicit air-sea momentum exchange in coupled atmosphere-
453 wave-ocean modeling of tropical cyclones. Ph.D. thesis. Citeseer.
- 454 Curcic, M., Chen, S.S., Özgökmen, T.M., 2016. Hurricane-induced ocean
455 waves and stokes drift and their impacts on surface transport and dispersion
456 in the Gulf of Mexico. Geophysical Research Letters 43, 2773–2781.
- 457 Curcic, M., Haus, B.K., 2020. Revised estimates of ocean surface drag in
458 strong winds. Geophysical Research Letters 47, e2020GL087647.
- 459 Dietrich, J., Bunya, S., Westerink, J., Ebersole, B., Smith, J., Atkinson,
460 J., Jensen, R., Resio, D., Luettich, R., Dawson, C., et al., 2010. A high-
461 resolution coupled riverine flow, tide, wind, wind wave, and storm surge
462 model for southern Louisiana and Mississippi. Part II: Synoptic description
463 and analysis of Hurricanes Katrina and Rita. Monthly Weather Review
464 138, 378–404.
- 465 Dietrich, J., Westerink, J., Kennedy, A., Smith, J., Jensen, R., Zijlema, M.,
466 Holthuijsen, L., Dawson, C., Luettich, R., Powell, M., et al., 2011. Hurricane
467 gustav (2008) waves and storm surge: Hindcast, synoptic analysis, and
468 validation in southern louisiana. Monthly Weather Review 139, 2488–2522.

- 469 Dietrich, J.C., Tanaka, S., Westerink, J.J., Dawson, C., Luettich, R., Zijlema,
470 M., Holthuijsen, L.H., Smith, J., Westerink, L., Westerink, H., 2012. Performance
471 of the unstructured-mesh, SWAN+ ADCIRC model in computing
472 hurricane waves and surge. *Journal of Scientific Computing* 52, 468–497.
- 473 Dobbelaere, T., Muller, E., Gramer, L., Holstein, D., Hanert, E., 2020a.
474 Report on the potential origin of the SCTLD in the Florida Reef Tract.
475 Available online at: [https://floridadep.gov/rcp/coral/documents/
476 report-potential-origin-sctld-florida-reef-tract](https://floridadep.gov/rcp/coral/documents/report-potential-origin-sctld-florida-reef-tract).
- 477 Dobbelaere, T., Muller, E.M., Gramer, L.J., Holstein, D.M., Hanert, E., 2020b.
478 Coupled epidemi-hydrodynamic modeling to understand the spread of a
479 deadly coral disease in Florida. *Frontiers in Marine Science* 7, 1016.
- 480 Donelan, M., Haus, B., Reul, N., Plant, W., Stiassnie, M., Graber, H., Brown,
481 O., Saltzman, E., 2004. On the limiting aerodynamic roughness of the
482 ocean in very strong winds. *Geophysical Research Letters* 31.
- 483 Drivdal, M., Broström, G., Christensen, K., 2014. Wave-induced mixing and
484 transport of buoyant particles: application to the statfjord a oil spill. *Ocean
485 Science* 10, 977–991.
- 486 Figueiredo, J., Baird, A.H., Connolly, S.R., 2013. Synthesizing larval com-
487 petence dynamics and reef-scale retention reveals a high potential for
488 self-recruitment in corals. *Ecology* 94, 650–659.
- 489 Frys, C., Saint-Amand, A., Le Hénaff, M., Figueiredo, J., Kuba, A., Walker,
490 B., Lambrechts, J., Vallaeys, V., Vincent, D., Hanert, E., 2020. Fine-scale
491 coral connectivity pathways in the Florida Reef Tract: implications for
492 conservation and restoration. *Frontiers in Marine Science* 7, 312.
- 493 Geuzaine, C., Remacle, J.F., 2009. Gmsh: A 3-d finite element mesh generator
494 with built-in pre-and post-processing facilities. *International journal for
495 numerical methods in engineering* 79, 1309–1331.

- 496 Harper, B., Kepert, J., Ginger, J., 2010. Guidelines for converting between
497 various wind averaging periods in tropical cyclone conditions. Citeseer.
- 498 Hegermiller, C.A., Warner, J.C., Olabarrieta, M., Sherwood, C.R., 2019.
499 Wave-current interaction between Hurricane Matthew wave fields and the
500 Gulf Stream. *Journal of Physical Oceanography* 49, 2883–2900.
- 501 Hoefel, F., Elgar, S., 2003. Wave-induced sediment transport and sandbar
502 migration. *Science* 299, 1885–1887.
- 503 Hoffmeister, J., Multer, H., 1968. Geology and origin of the Florida Keys.
504 Geological Society of America Bulletin 79, 1487–1502.
- 505 Holthuijsen, L.H., Powell, M.D., Pietrzak, J.D., 2012. Wind and waves in
506 extreme hurricanes. *Journal of Geophysical Research: Oceans* 117.
- 507 Janssen, P.A., 1991. Quasi-linear theory of wind-wave generation applied to
508 wave forecasting. *Journal of physical oceanography* 21, 1631–1642.
- 509 Johns, W.E., Schott, F., 1987. Meandering and transport variations of the
510 Florida Current. *Journal of physical oceanography* 17, 1128–1147.
- 511 Knaff, J.A., Sampson, C.R., Musgrave, K.D., 2018. Statistical tropical cyclone
512 wind radii prediction using climatology and persistence: Updates for the
513 western North Pacific. *Weather and Forecasting* 33, 1093–1098.
- 514 Knutson, T.R., McBride, J.L., Chan, J., Emanuel, K., Holland, G., Landsea,
515 C., Held, I., Kossin, J.P., Srivastava, A., Sugi, M., 2010. Tropical cyclones
516 and climate change. *Nature geoscience* 3, 157–163.
- 517 Komen, G., Hasselmann, S., Hasselmann, K., 1984. On the existence of a
518 fully developed wind-sea spectrum. *Journal of physical oceanography* 14,
519 1271–1285.

- 520 Kourafalou, V.H., Kang, H., 2012. Florida Current meandering and evo-
521 lution of cyclonic eddies along the Florida Keys Reef Tract: Are they
522 interconnected? *Journal of Geophysical Research: Oceans* 117.
- 523 Kundu, P.K., 1976. Ekman veering observed near the ocean bottom. *Journal*
524 *of Physical Oceanography* 6, 238–242.
- 525 Landsea, C.W., Franklin, J.L., 2013. Atlantic hurricane database uncertainty
526 and presentation of a new database format. *Monthly Weather Review* 141,
527 3576–3592.
- 528 Lane, E.M., Restrepo, J., McWilliams, J.C., 2007. Wave-current interaction:
529 A comparison of radiation-stress and vortex-force representations. *Journal*
530 *of physical oceanography* 37, 1122–1141.
- 531 Langmuir, I., 1938. Surface motion of water induced by wind. *Science* 87,
532 119–123.
- 533 Le Hénaff, M., Kourafalou, V.H., Paris, C.B., Helgers, J., Aman, Z.M., Hogan,
534 P.J., Srinivasan, A., 2012. Surface evolution of the Deepwater Horizon
535 oil spill patch: combined effects of circulation and wind-induced drift.
536 *Environmental science & technology* 46, 7267–7273.
- 537 Lee, T.N., Leaman, K., Williams, E., Berger, T., Atkinson, L., 1995. Florida
538 Current meanders and gyre formation in the southern Straits of Florida.
539 *Journal of Geophysical Research: Oceans* 100, 8607–8620.
- 540 Lee, T.N., Mayer, D.A., 1977. Low-frequency current variability and spin-off
541 eddies along the shelf off southeast Florida. *Collected Reprints* 1, 344.
- 542 Lee, T.N., Smith, N., 2002. Volume transport variability through the Florida
543 Keys tidal channels. *Continental Shelf Research* 22, 1361–1377.
- 544 Lee, T.N., Williams, E., 1988. Wind-forced transport fluctuations of the
545 Florida Current. *Journal of Physical Oceanography* 18, 937–946.

- 546 Li, Z., Johns, B., 1998. A three-dimensional numerical model of surface
547 waves in the surf zone and longshore current generation over a plane beach.
548 *Estuarine, Coastal and Shelf Science* 47, 395–413.
- 549 Lidz, B.H., Shinn, E.A., 1991. Paleoshorelines, reefs, and a rising sea: South
550 florida, usa. *Journal of Coastal Research* , 203–229.
- 551 Lin, N., Chavas, D., 2012. On hurricane parametric wind and applications in
552 storm surge modeling. *Journal of Geophysical Research: Atmospheres* 117.
- 553 Liu, Y., Weisberg, R.H., 2012. Seasonal variability on the West Florida shelf.
554 *Progress in Oceanography* 104, 80–98.
- 555 Liu, Y., Weisberg, R.H., Zheng, L., 2020. Impacts of hurricane Irma on the
556 circulation and transport in Florida Bay and the Charlotte Harbor estuary.
557 *Estuaries and Coasts* 43, 1194–1216.
- 558 Liubartseva, S., Coppini, G., Lecci, R., Clementi, E., 2018. Tracking plastics
559 in the Mediterranean: 2D Lagrangian model. *Marine pollution bulletin*
560 129, 151–162.
- 561 Longuet-Higgins, M.S., 1970. Longshore currents generated by obliquely
562 incident sea waves. *Journal of geophysical research* 75, 6778–6789.
- 563 Longuet-Higgins, M.S., Stewart, R., 1964. Radiation stresses in water waves;
564 a physical discussion, with applications, in: Deep sea research and oceano-
565 graphic abstracts, Elsevier. pp. 529–562.
- 566 Lugo-Fernández, A., Deslarzes, K.J., Price, J.M., Boland, G.S., Morin, M.V.,
567 2001. Inferring probable dispersal of Flower Garden Banks coral larvae (Gulf
568 of Mexico) using observed and simulated drifter trajectories. *Continental
569 Shelf Research* 21, 47–67.
- 570 Madsen, O.S., Poon, Y.K., Gruber, H.C., 1989. Spectral wave attenuation by
571 bottom friction: Theory, in: *Coastal Engineering* 1988, pp. 492–504.

- 572 Malmstadt, J., Scheitlin, K., Elsner, J., 2009. Florida hurricanes and damage
573 costs. *southeastern geographer* 49, 108–131.
- 574 Marsooli, R., Lin, N., Emanuel, K., Feng, K., 2019. Climate change ex-
575 acerbates hurricane flood hazards along US Atlantic and Gulf Coasts in
576 spatially varying patterns. *Nature communications* 10, 1–9.
- 577 McWILLIAMS, J.C., Restrepo, J.M., Lane, E.M., 2004. An asymptotic theory
578 for the interaction of waves and currents in coastal waters. *Journal of Fluid*
579 *Mechanics* 511, 135.
- 580 McWilliams, J.C., Sullivan, P.P., 2000. Vertical mixing by Langmuir circula-
581 tions. *Spill Science & Technology Bulletin* 6, 225–237.
- 582 Mei, C.C., 1989. The applied dynamics of ocean surface waves. volume 1.
583 World scientific.
- 584 Moon, I.J., Ginis, I., Hara, T., Thomas, B., 2007. A physics-based parame-
585 terization of air-sea momentum flux at high wind speeds and its impact on
586 hurricane intensity predictions. *Monthly weather review* 135, 2869–2878.
- 587 Pinelli, J.P., Roueche, D., Kijewski-Correa, T., Plaz, F., Prevatt, D., Zisis,
588 I., Elawady, A., Haan, F., Pei, S., Gurley, K., et al., 2018. Overview of
589 damage observed in regional construction during the passage of Hurricane
590 Irma over the State of Florida, in: *Forensic Engineering 2018: Forging*
591 *Forensic Frontiers*. American Society of Civil Engineers Reston, VA, pp.
592 1028–1038.
- 593 Powell, M.D., Houston, S.H., Amat, L.R., Morisseau-Leroy, N., 1998. The
594 HRD real-time hurricane wind analysis system. *Journal of Wind Engineering*
595 and Industrial Aerodynamics 77, 53–64.
- 596 Powell, M.D., Vickery, P.J., Reinhold, T.A., 2003. Reduced drag coefficient
597 for high wind speeds in tropical cyclones. *Nature* 422, 279–283.

- 598 Röhrs, J., Christensen, K.H., Hole, L.R., Broström, G., Drivdal, M., Sundby,
599 S., 2012. Observation-based evaluation of surface wave effects on currents
600 and trajectory forecasts. *Ocean Dynamics* 62, 1519–1533.
- 601 Schott, F.A., Lee, T.N., Zantopp, R., 1988. Variability of structure and
602 transport of the Florida Current in the period range of days to seasonal.
603 *Journal of Physical Oceanography* 18, 1209–1230.
- 604 Shinn, E.A., 1988. The geology of the Florida Keys. *Oceanus* 31, 46–53.
- 605 Siadatmousavi, S.M., Jose, F., Stone, G., 2011. Evaluation of two WAM
606 white capping parameterizations using parallel unstructured SWAN with
607 application to the Northern Gulf of Mexico, USA. *Applied Ocean Research*
608 33, 23–30.
- 609 Sikirić, M.D., Roland, A., Janečković, I., Tomazić, I., Kuzmić, M., 2013.
610 Coupling of the Regional Ocean Modeling System (roms) and Wind Wave
611 Model. *Ocean Modelling* 72, 59–73.
- 612 Smith, N.P., 1982. Response of Florida Atlantic shelf waters to hurricane
613 David. *Journal of Geophysical Research: Oceans* 87, 2007–2016.
- 614 Stokes, G.G., 1880. On the theory of oscillatory waves. *Transactions of the*
615 *Cambridge philosophical society* .
- 616 Tolman, H.L., et al., 2009. User manual and system documentation of
617 WAVEWATCH III TM version 3.14. Technical note, MMAB Contribution
618 276, 220.
- 619 Van Den Bremer, T., Breivik, Ø., 2018. Stokes drift. *Philosophical Trans-*
620 *actions of the Royal Society A: Mathematical, Physical and Engineering*
621 *Sciences* 376, 20170104.
- 622 Villas Bôas, A.B., Cornuelle, B.D., Mazloff, M.R., Gille, S.T., Arduin, F.,
623 2020. Wave–current interactions at meso-and submesoscales: Insights from

- 624 idealized numerical simulations. *Journal of Physical Oceanography* 50,
625 3483–3500.
- 626 Weisberg, R., Liu, Y., Mayer, D., 2009. Mean circulation on the west Florida
627 continental shelf observed with long-term moorings. *Geophys. Res. Lett*
628 36, L19610.
- 629 Weisberg, R.H., Zheng, L., 2006. Hurricane storm surge simulations for
630 Tampa Bay. *Estuaries and Coasts* 29, 899–913.
- 631 Wu, L., Chen, C., Guo, P., Shi, M., Qi, J., Ge, J., 2011. A FVCOM-
632 based unstructured grid wave, current, sediment transport model, I. Model
633 description and validation. *Journal of Ocean University of China* 10, 1–8.
- 634 Xian, S., Feng, K., Lin, N., Marsooli, R., Chavas, D., Chen, J., Hatzikyriakou,
635 A., 2018. Brief communication: Rapid assessment of damaged residential
636 buildings in the Florida Keys after Hurricane Irma. *Natural Hazards and*
637 *Earth System Sciences* 18, 2041–2045.
- 638 Zedler, S., Niiler, P., Stammer, D., Terrill, E., Morzel, J., 2009. Ocean's
639 response to Hurricane Frances and its implications for drag coefficient
640 parameterization at high wind speeds. *Journal of Geophysical Research: Oceans* 114.
- 642 Zhang, C., Durgan, S.D., Lagomasino, D., 2019. Modeling risk of mangroves
643 to tropical cyclones: A case study of Hurricane Irma. *Estuarine, Coastal*
644 *and Shelf Science* 224, 108–116.